OPEN ACCESS

# Submonolayer growth of copper-phthalocyanine on Ag(111)

New Journal of Physics
The open-access journal for physics

# Submonolayer growth of copper-phthalocyanine on Ag(111)

**Ingo Kröger[1], Benjamin Stadtmüller[1], Christoph Stadler[2], Johannes Ziroff[3], Mario Kochler[3], Andreas Stahl[2], Florian Pollinger[2,5], Tien-Lin Lee[4,6], Jörg Zegenhagen[4], Friedrich Reinert[3] and Christian Kumpf[1,7]**

[1] Institut für Bio- and Nanosysteme (IBN-3), Forschungszentrum Jülich GmbH, D-52425 Jülich, Germany and JARA (Jülich Aachen Research Alliance)-Future Information Technology
[2] Experimentelle Physik II, Universität Würzburg, Am Hubland, D-97074 Würzburg, Germany
[3] Experimentelle Physik VII, Universität Würzburg, Am Hubland, D-97074 Würzburg, Germany
[4] European Synchrotron Radiation Facility, BP220, 38043 Grenoble Cedex, France
E-mail: c.kumpf@fz-juelich.de

*New Journal of Physics* **12** (2010) 083038 (23pp)
Received 28 May 2010
Published 17 August 2010
Online at http://www.njp.org/
doi:10.1088/1367-2630/12/8/083038

**Abstract.** The growth of high-quality thin films is a key issue in the ability to design electronic devices based on organic materials and to tune their properties. In this context, the interfaces between metals and organic films play a decisive role. Here, we report on the interface formation between copper-phthalocyanine (CuPc) and an Ag(111) surface using various complementary methods. High-resolution low-energy electron diffraction revealed a rich phase diagram for this system with disordered (two-dimensional (2D)-gas-like) and ordered structures (commensurate and point-on-line). In particular, a *continuous* change in lattice parameters with increasing coverage was found for long-range ordered structures, indicating a substrate-mediated *repulsive* intermolecular interaction similar to the case of tin-phthalocyanine/Ag(111). Chemisorptive

[5] Present address: Physikalisch-Technische Bundesanstalt, Bundesallee 100, 38116 Braunschweig, Germany.
[6] Present address: Diamond Light Source Ltd, Diamond House, Harwell Science and Innovation Campus, Didcot, Oxfordshire OX11 0DE, UK.
[7] Author to whom any correspondence should be addressed.

bonding to the substrate was found by x-ray standing waves and ultraviolet photoelectron spectroscopy, and this weakened with increasing coverage at low temperature. This remarkable effect is correlated to a shift in the highest occupied molecular orbital (HOMO) and a HOMO-1 split off band to higher binding energies. Based on our experimental results, we present a comprehensive study of the adsorption behavior of CuPc/Ag(111), including the mechanisms for phase formation and molecular interaction.

**Contents**



## 1. Introduction

The growth of organic thin films on metallic substrates has become a major field of interest for the organic electronics and surface science community. Understanding and—consequently—controlling the layer properties is the main issue in successfully designing organic semiconductor devices (organic light emitting diodes (OLEDs), organic field effect transistors (OFETs), organic solar cells, etc). Organic–inorganic interfaces play an important role in this context, since their formation as well as their geometric, electronic and possibly also spintronic properties define the characteristics of the films and devices. Therefore, the formation of the first molecular layer on a metallic surface, which acts as a template for multilayer growth, is the subject of many recent investigations.

Regarding the nature of organic–metallic bonding, noble metal surfaces represent the most interesting choice because of their medium interaction strength with adsorbates, which stems from a sophisticated interplay of weak chemisorption and van der Waals forces. This prevents dissociation and enables high mobility of the molecules on the surface, but also allows electronic interaction with the surface. The consequence is the general phenomenon of island formation in the sub-monolayer (sub-ML) regime, since usually attractive intermolecular forces in combination with high mobility lead to clustering of molecules. Due to the complexity

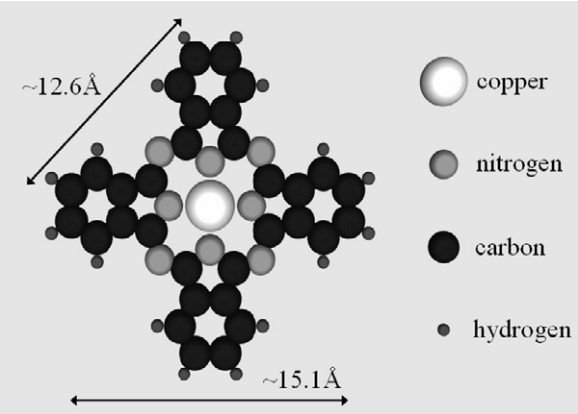


**Figure 1.** Atomic model of the copper-phthalocyanine molecule $CuC_{32}N_8H_{16}$.

of substrate–molecule and molecule–molecule interactions, $\pi$-conjugated molecules show a diversity of phases that can strongly depend on coverage, temperature, substrate and film preparation parameters [1, 2], as well as the shape of the molecule and possible reactive side groups. A systematically studied prototype for these kinds of model systems is 3,4,9,10-perylene tetracarboxylicacid-dianhydride (PTCDA) on Ag(111) (see [1], [3]–[9] and references therein).

In contrast to these investigations, we studied the adsorption of a molecule *without* reactive side groups. The focus of this paper are the structural properties of sub-ML films of metal-phthalocyanines (MePc). These molecules are already widely used as organic semiconductors because of their p-type conductivity and high photoconductive sensitivity in the near-infrared region. They consist of an aromatic body with a metal atom bound in its center (see figure 1).

Depending on the central metal atom, the molecular geometry can be modified from planar ($H_2$Pc and CuPc) to non-planar (SnPc and TiOPc) configurations. Consequently, the molecules have different bulk structures [10]. Furthermore, different MePc molecules have different electronic properties, such as, most prominently, different vertical dipole moments. In earlier work, we investigated the lateral and vertical structures of the non-planar SnPc adsorbed on Ag(111) in detail [11, 12], and we observed a substrate-mediated intermolecular repulsion in the sub-ML regime and a dilute sub-ML growth mode instead of classical island growth. In this paper, we present a study of the planar copper-phthalocyanine on Ag(111) using complementary methods. We have investigated the correlation between different lateral geometric structures (two-dimensional (2D)-gas, commensurate, point-on-line (p.o.l.)), adsorption heights and bonding distances as well as the electronic valence structure. The experiments were performed using spot profile analysis–low-energy electron diffraction (SPA–LEED), normal incidence x-ray standing waves (NIXSW) and ultraviolet photoelectron spectroscopy (UPS). These methods allow us to understand this system comprehensively, and to qualify and quantify the correlations between the geometric and the electronic structure. We successfully elucidated the growth mechanism in the sub-ML regime, which differs fundamentally from common island growth of other $\pi$-conjugated molecules.

This paper is organized as follows. First, we give a short introduction to sample preparation and experimental methods. In the following section, the SPA–LEED results (lateral structure and phase diagram), NIXSW results (vertical structure) and UPS results (electronic structure) are illustrated and discussed. The last section concludes and discusses the complete picture of the adsorption of CuPc/Ag(111).

## 2. Experimental

### 2.1. Sample preparation

The Ag(111) sample was prepared by argon sputtering (500 eV, $\pm 50^{\circ}$ incident angle) and subsequent annealing at 723 K. This procedure was proven to lead to large surface terraces ($\geqslant$500 Å, obtained from SPA–LEED peak widths) and very high crystalline quality of the surface. Since this is an important topological aspect that can influence the growth behavior of organic thin films, we always used identical surface preparation parameters in order to obtain identical conditions for all film depositions reported in this paper. Deposition was performed by evaporating previously sublimated copper(II)-phthalocyanine (CuPc) from a home-made Knudsen cell. The evaporation rate was observed using a quadrupole mass spectrometer. During the process, the sample was kept at room temperature. Post deposition annealing at 533 K for 20 min was always performed and turned out to be crucial in order to guarantee homogeneous coverage of the CuPc molecules on all silver terraces. Longer annealing or annealing at higher temperatures leads to desorption of the molecules (which already indicates a relatively weak bonding). The coverage was finally determined by x-ray photoelectron spectroscopy (XPS) using the net C1s peak integral (after linear background correction), taking the net C1s integral of the ML structure as a reference (see section 3). The accuracy of this method was determined to be $\pm$0.08 ML (for a precise calibration of the coverage of 1 ML, see below). In order to avoid falsifications of SPA–LEED measurements by XPS-induced beam damage, we always performed the XPS after the SPA–LEED measurements. For ordered structures, we also used SPA–LEED images to obtain the size of the unit cells. Due to a repulsive intermolecular interaction that causes homogeneous filling of the surface (see below), this enables a very precise way of coverage determination (see section 3).

### 2.2. Spot profile analysis–low energy electron diffraction (SPA–LEED)

SPA–LEED combines a high k-resolution (transfer width $\geqslant$540 Å) with a high dynamic range of the detector (1–$10^6$ cps) [13]. Due to its high resolution, the method can be used for a precise determination of unit cell sizes. We used it for a complete determination of the phase diagram in the sub-ML range. All measurements were performed in a UHV chamber with a base pressure below $5 \times 10^{-10}$ mbar. From the SPA–LEED images, we determined epitaxy matrices for the CuPc superstructures by comparison with calculated diffraction patterns using kinematical theory. Calibration was performed using a well-known commensurate structure (NTCDA/Ag(111)). The accuracy of this method is approximately 0.04 for each matrix entry for absolute structure determination and 0.02 for relative structure determination, i.e. when two similar structures should be distinguished.

### 2.3. The normal incidence x-ray standing wave (NIXSW) technique

The NIXSW technique allows us to determine vertical bonding distances of an adsorbate on a crystal surface with high accuracy ($10^{-2}$ Å). It is successfully applied to investigate adsorption heights and distortion of molecules upon adsorption (e.g. PTCDA [3, 4, 6, 14], NTCDA [15, 16], SnPc [12], $F_{16}$CuPc [17], $C_{22}H_{14}$ [18] and azobenzene [19]). We performed the NIXSW experiments at beamline ID32 of the European Synchrotron Radiation Facility (ESRF) in Grenoble, France. All the equipment necessary for sample preparation is available at

that beamline, as well as a LEED optics and a hemispherical electron analyzer ($r = 150$ mm), which is mounted with an angle of 45° relative to the incident synchrotron beam. The base pressure during the experiments was below $5 \times 10^{-10}$ mbar. We will now briefly introduce the basics of this method; a more detailed description can be found elsewhere [20]–[22].

An x-ray standing wave field is generated by the coherent superposition of an impinging monochromatic x-ray plane wave $\vec{E}_0$ on a crystal surface and its Bragg reflected wave $\vec{E}_H$, when the Bragg condition for an $\vec{H} = (hkl)$ reflection is fulfilled: $\vec{H} = \vec{k}_H - \vec{k}_0$. The standing wave field with intensity $I(E, \vec{r})$ represents a modulation of the electric field perpendicular to the Bragg planes with a periodicity $d_H$ that is identical to the lattice spacing $d_\mathrm{H}$ of the substrate crystal,

$$I(E, \vec{r}) = |E_0|^2 \left[ 1 + R(E) + 2\sqrt{R(E)} \cdot \cos\left(\nu(E) + \vec{H} \cdot \vec{r}\right) \right], \tag{1}$$

whereby $R(E) = |E_\mathrm{H}/E_0|^2$ is the reflectivity function and $\nu$ the phase of the complex field amplitude ratio $E_\mathrm{H}/E_0 = \sqrt{R} \cdot \mathrm{e}^{\mathrm{i}\nu}$. The scalar product simplifies to $\vec{H} \cdot \vec{r} = 2\pi(D_\mathrm{H}/d_\mathrm{H})$ and indicates the periodicity of the standing wave. Upon scanning the photon energy through the Bragg condition, the phase of the complex field amplitudes $\nu$ changes from $\pi$ to 0, which makes the standing wave field move through the crystal by half of the lattice spacing $d_\mathrm{H}$. This move causes a modulation of the photoemission (PE) yield from any atomic species in the crystal and at its surface, since the photon absorption of the atoms is directly proportional to the intensity of the electric field at their position. Hence, a characteristic PE yield curve is measured by such a scan through the Bragg condition for each atomic species. The shape of the yield curve strongly depends on the position $D_\mathrm{H}$ of the species relative to the substrate Bragg planes. In combination with XPS, the method is element specific and can resolve the geometry of an adsorbed molecule.

In the case of multiple adsorption sites for one atomic species, the parameter 'coherent fraction' $F^\mathrm{H}$ must be introduced. Coherent fraction $F^\mathrm{H}$ and coherent position $P^\mathrm{H} = D_\mathrm{H}/d_\mathrm{H}$ can be understood as the amplitude and phase of the H-Fourier component of the spatial distribution of an adsorbate, where each single adsorbate atom $m$ has a fraction of $F_m^\mathrm{H} = 1$ and a position $P_m^\mathrm{H}$.

$$F^\mathrm{H} \exp(\mathrm{i}2\pi P^\mathrm{H}) = \sum_{m=1}^{N} \frac{F_m^\mathrm{H}}{N} \exp\left(\mathrm{i}2\pi P_m^\mathrm{H}\right). \tag{2}$$

In NIXSW experiments, the photon energy is determined by the Bragg condition that must be fulfilled for the given substrate crystal structure and a Bragg angle of (close to) 90°. This usually results in photon energies that are relatively high for PE. Hence, the dipole approximation is often not sufficient to describe the PE process. To express the XSW photoelectron yield, multipole correction parameters $Q$ [23, 24], $\Delta$ and $\Psi = \tan^{-1}(Q \tan \Delta)$ must be introduced. This leads to the final formula for the XSW PE yield that is used for fitting the experimental data. This contains the two parameters $F^\mathrm{H}$ and $P^\mathrm{H}$, which represent the main result of an XSW experiment (for each atomic species of interest),

$$I(E) = 1 + \frac{1+Q}{1-Q} R + 2\sqrt{R} \cdot F^\mathrm{H} \frac{\sqrt{1 + Q^2 \tan^2 \Delta}}{1-Q} \cos\left(\nu - \Psi + 2\pi P^\mathrm{H}\right). \tag{3}$$

The formula demonstrates that the $Q$ parameter can be derived from fitting XSW profiles if it is known that the coherent fraction $F^\mathrm{H}$ is zero. This is the case for a thick, disordered multilayer film. We have measured the $Q$ parameter using films with a thickness of $\geqslant$20 ML,

**Table 1.** Multipole correction parameters of the investigated elements.

| | C1s | N1s | $Cu2p_{3/2}$ |
|---|---|---|---|
| $Q$ | 0.24(2) [12] | 0.22(2) [12] | 0.17(2) |
| $\Delta$ | −0.21 [12] | −0.26 [12] | −0.21 |

which were prepared at $T_{\text{sample}} = 150\,\text{K}$ (see table 1). For thinner films, we observed that the layer is not 'disordered enough'. The values for $\Delta$ are taken from [12].

### *2.4. Ultraviolet photoelectron spectroscopy (UPS)*

The ultraviolet photoelectron spectroscopy (UPS) measurements were performed with a SCIENTA R4000 analyser combined with a monochromatized, microwave-driven $\text{He} - \text{I}_\alpha$ source ($h\nu = 21.23\,\text{eV}$). The spectra were taken at a base pressure of $1 \times 10^{-10}$ mbar, increasing to values $\leqslant 1 \times 10^{-9}$ mbar due to the He-leakage, with a net energy resolution of 6 meV. We used a geometry with the incident photon beam, axis of sample rotation and analyzer (direction of photoelectron detection) lying in one plane. The angle between the incident beam and the analyzer was 45°, and that between the sample rotation axis and the analyzer was 90°. The detection angle between the surface normal and the analyzer was around 50°, optimized for the PE intensity of the molecular orbitals.

## 3. Spot profle analysis–low-energy electron diffraction (SPA–LEED) investigations

Our SPA–LEED investigation revealed that the phase diagram of CuPc/Ag(111) can be divided into three regimes: the gaseous 'g-phases' and the p.o.l. phases, including the ML structure and the commensurate c-phase (see figure 2). We describe the properties of each regime of the phase diagram in detail in the following, beginning with the high coverage regime between 0.89 and 1.00 ML.

The ML structure can easily be prepared by annealing a multilayer film at 533 K for 20 min. It has the smallest unit cell of all ordered structures and was taken as a reference for the coverages obtained by XPS and SPA–LEED (i.e. all coverages in this paper are given relative to the ML structure, which has an absolute coverage of 0.521 molecules $\text{nm}^{-2}$). Reducing the coverage by depositing fewer molecules or by annealing at temperatures above 533 K leads to a *continuous* change in the diffraction pattern (see figure 3). This was confirmed by investigating 25 different structures in the coverage regime from 0.9 to 1.0 ML, which all have a different unit cell. Their parameters (length of the unit cell vectors and their angles to the fundamental crystallographic directions of the substrate) are displayed in figure 4. The continuous change can easily be seen.

In the right part of figure 4, the positions of the corners of superlattice cells on the Ag(111) surface lattice are indicated as small circles for different coverages. It can be seen that all superlattice points lie on intercepting lines of the substrate lattice points. This is called a p.o.l. coincidence [25, 26], which is often observed in organic adsorbate systems on weakly interacting substrates, such as PTCDA on HOPG [25] and Au(111) [27], TiOPc on Au(111) [28], and NTCDA on HOPG and $MoS_2$ [29]. In a theoretical approach based on van der

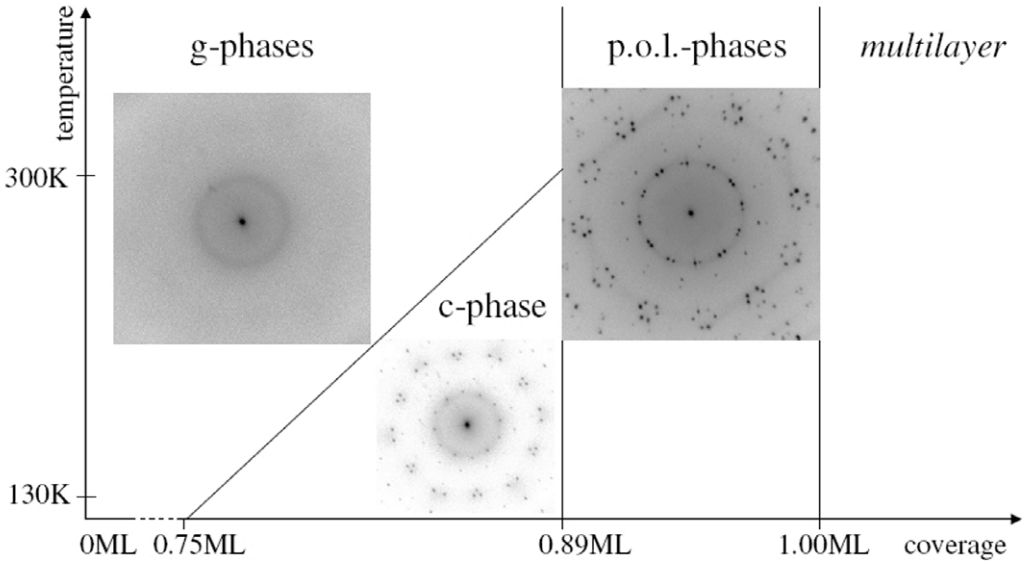


**Figure 2.** Phase diagram of CuPc/Ag(111). Three different regions (gas-like, commensurate and point-on-line (p.o.l.) phases) are indicated versus temperature and coverage. The insets represent typical SPA–LEED images for the corresponding phases ($E = 45$ eV, 2.2 Å$^{-1}$ × 2.2 Å$^{-1}$ displayed).

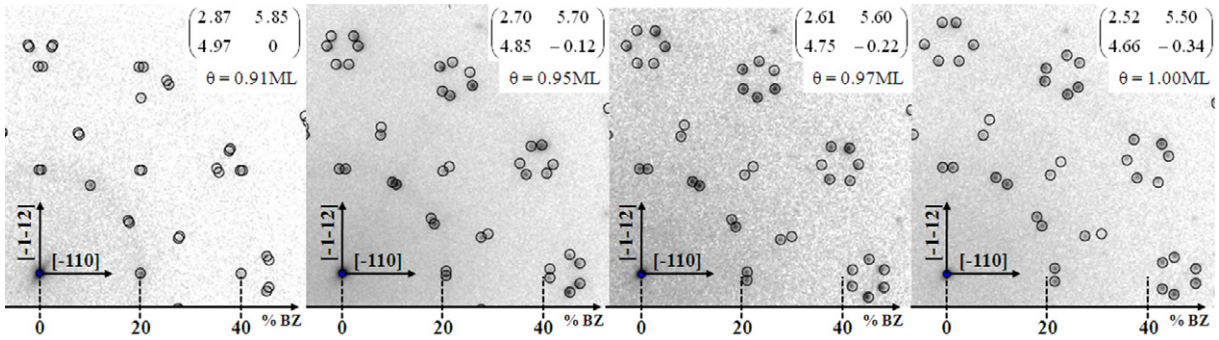


**Figure 3.** SPA–LEED diffraction pattern ($E = 45$ eV) of p.o.l. phases including the ML structure. Circles indicate the positions of diffraction spots calculated from the epitaxy matrices. The coverage is also displayed in the upper right corner.

Waals interaction, Mannsfeld *et al* [28, 30] showed that the formation of a p.o.l. coincidence reduces the interface potential energy. Therefore—in general—it can be considered as a case of epitaxy, similar to commensurate (point-on-point) coincidence. However, in the case of CuPc on Ag(111), a pure van der Waals approach is not sufficient for a realistic energetic consideration since the substrate is more reactive and the molecule–substrate interaction is dominated by chemisorption.

From the right part of figure 4 it can also be seen that the unit cell expands continuously from $191.8 \pm 1.5$ Å$^2$ at 1.0 ML to $217.2 \pm 1.5$ Å$^2$ at 0.89 ML. This result indicates a repulsive molecule–molecule interaction within the long-range ordered molecular 2D crystal that is

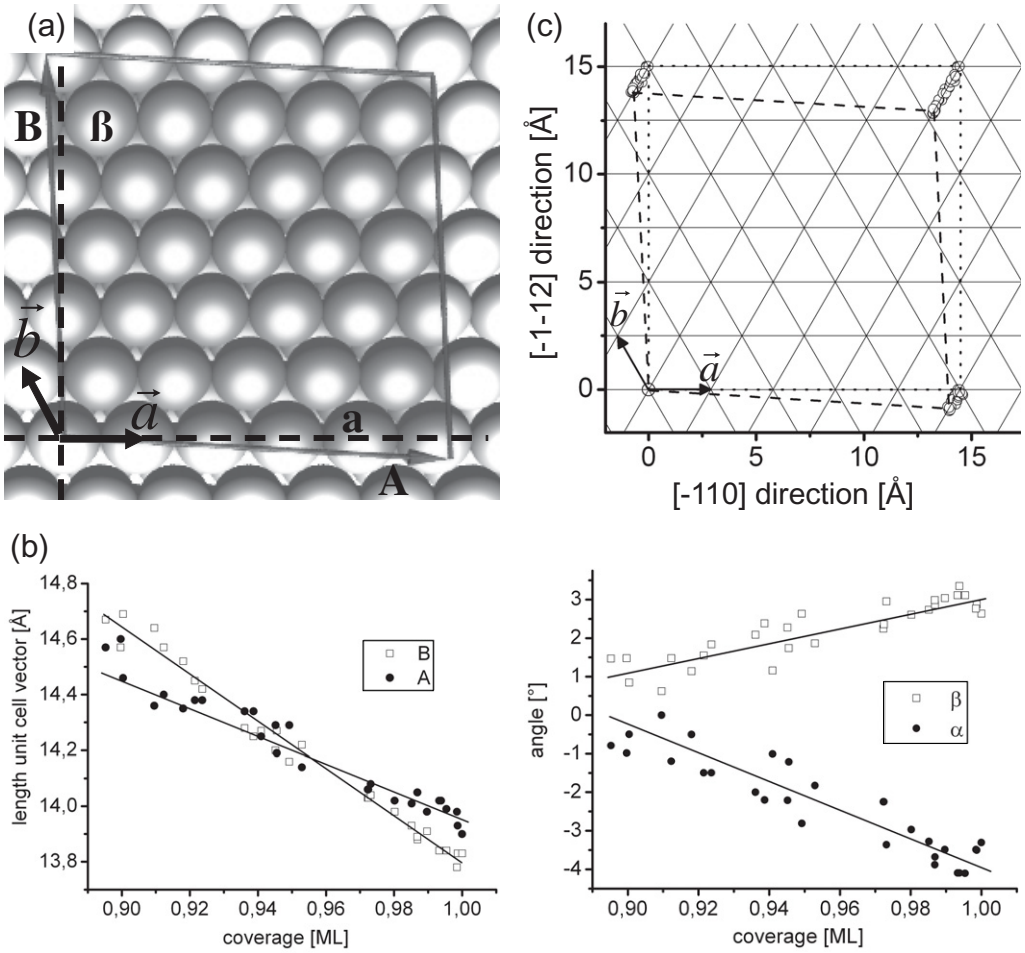


**Figure 4.** (a) Definition of unit supercell parameters: unit cell vectors $\vec{A}$ and $\vec{B}$ and their angles to high-symmetry directions of the substrates $\alpha$ and $\beta$. (b) Continuous change of unit vector lengths and orientation angles with increasing coverage in the p.o.l. phases. The accuracy is $\pm 0.12$ Å and $\pm 0.5^{\circ}$ for vector lengths and angles, respectively. (c) Circles indicate the positions of the corners of the supercells on the Ag(111) lattice for different coverages (dashed line: 1.00 ML; dotted line: 0.89 ML). $\vec{a}$ and $\vec{b}$ are the unit vectors of the Ag(111) substrate lattice.

unaffected by a change in the temperature in the range of 130–300 K. To our knowledge, such a continuous change in lattice parameters for a molecular crystal was not reported previous to our earlier paper on Sn-phthalocyanine on Ag(111) [11]. This is in strong contrast to the commonly known growth mode of $\pi$-conjugated molecules forming islands of different well-defined structures.

Due to this repulsive interaction, the adsorbate layer is closed in the entire p.o.l. coverage regime, since all surface terraces are homogenously filled, and neither island formation nor uncovered Ag(111) surface areas occur. As mentioned above, this allows a much more precise coverage determination than XPS, since the unit cell contains one molecule and hence its size can be interpreted as the 'surface area per molecule', i.e. the inverse coverage. We estimated the precision of this method to $\pm 0.02$ ML.

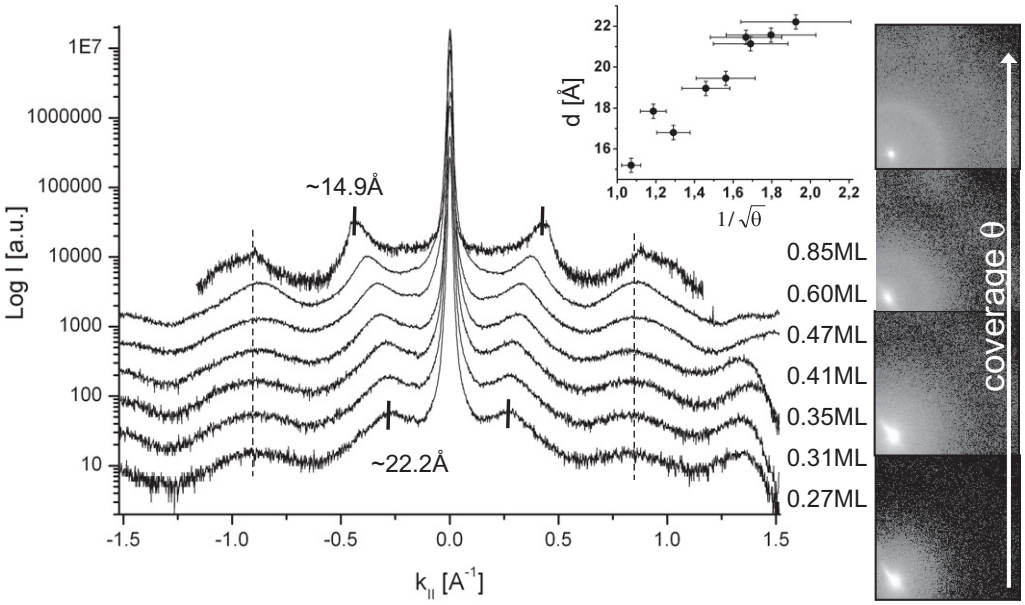


**Figure 5.** Radial line scans through the SPA–LEED images obtained at different coverages. Average intermolecular distances were derived from the positions of the first peaks at about $\pm 0.3$–$0.4\,\text{Å}^{-1}$, which corresponds to the radius of the inner ring. Right: corresponding 2D images. The inset shows the average molecule–molecule distance plotted versus the inverse square root of the coverage, which is proportional to the area per molecule.

If we decrease the coverage below $\approx 0.89$ ML, sharp spots can no longer be observed in the LEED images at room temperature, indicating the absence of crystalline long range order. Instead, two diffuse rings are observed. They are visible in the LEED images in figure 5, and more clearly as peaks in the corresponding line scans.

With decreasing coverage, the inner ring becomes broader and its radius decreases continuously. This ring represents the scattering intensity from a disordered structure with a relatively well-defined intermolecular distance. The ring radius reflects this nearest-neighbor distance $d$ within the overlayer that can be considered as a molecular 2D gas. The denser it becomes, the better defined the nearest-neighbor distance $d$ is, which makes the ring sharper and also stronger in intensity. In such a 2D gas, $d^2$ should be proportional to the area per molecule, i.e. to the inverse coverage $1/\theta$. This linear dependence is confirmed by the data shown in the inset of figure 5.

The fact that the molecules in the g-phase maximize the distance to their neighbors could be interpreted as intermolecular repulsion. However, we cannot rule out the effect of entropy in this context, since the overlayer is disordered. So a simple entropy effect might be responsible for the apparent repulsive molecule–molecule interaction in the gas phase. However, the occurrence of gas-like phases at least demonstrates the absence of a dominant attractive intermolecular interaction, since no island formation was observed.

The second ring observed in the SPA–LEED pattern has a radius remaining constant with coverage. Hence, it cannot be interpreted as the second diffraction order of the inner ring. Actually, the absence of a second-order ring indicates that this phase is highly disordered and justifies the term ‘2D gas’ (g-phase). The real-space distance corresponding to the second

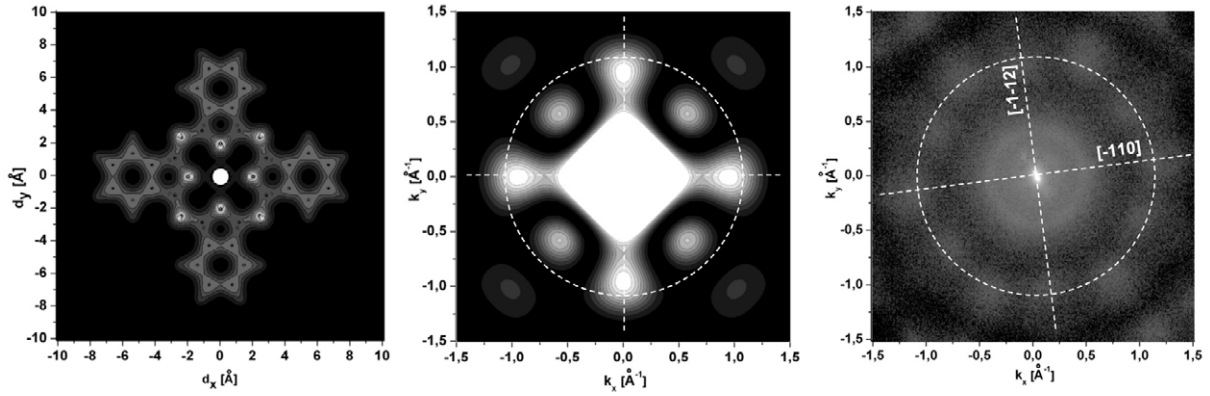


**Figure 6.** Left: DFT calculation of the total electron density of CuPc (gas-phase calculation [31] using the B3-LYP functional and a LANL2DZ basis set). Middle: its Fourier transform. Right: measured SPA–LEED image of the g-phase ($d \approx 16.8$ Å) at 127 K.

ring radius is $7.5 \pm 1.1$ Å, which represents a prominent distance within the molecule. At low temperature, the ring shows a 12-fold azimuthal intensity modulation with maxima in the [-110], [0-11], [10-1], [-1-12], [2-1-1] and [-12-1] directions (see figure 6, right).

In order to prove the argument of intramolecular scattering, we calculated the total electron density for a free molecule and the corresponding Fourier transform that represents the molecular scattering intensity in reciprocal space (left and central parts of figure 6, respectively). The calculations show four intensity maxima in the directions along the molecular wings with a $k$ value, in good agreement with the ring radius in the experimental data. A superposition of three molecular orientations rotated by 120° (according to the 3-fold symmetry of the Ag(111) substrate) leads to the experimentally observed 12 intensity maxima at low temperature. This proves that below $T = 140$ K, the CuPc molecules show an azimuthal alignment of the molecular wings along the [-110], [0-11] and [10-1] directions of the substrate. In contrast, at room temperature, the molecules have a random azimuthal alignment indicated by a homogeneous intensity distribution of the outer ring. We relate this observation to a condensation of the molecules into the energetically most favorable adsorption sites at low temperatures, leading to the discussed geometrical alignment with the substrate.

In a small coverage regime between $\approx 0.75$ and $\approx 0.89$ ML, a phase transition from g-phases to a commensurate superlattice (c-phase) can be observed. It occurs only when the average intermolecular distance $d$ in the disordered g-phase is smaller than $\approx 16$ Å, i.e. at sufficiently high coverage. This c-phase corresponds to the lower coverage limit of the p.o.l. phases with the epitaxy matrix

$$\begin{pmatrix} 3 & 6 \\ 5 & 0 \end{pmatrix} \tag{4}$$

and a rectangular (almost squared) unit cell. It also has one molecule per unit cell. For SnPc/Ag(111), a similar phase transition was found [11] with two molecules per unit cell, one in Sn-up and the other in Sn-down position. This phase transition was interpreted as a switching from (overall) repulsive to attractive intermolecular interaction caused by an additional site-specific molecule–substrate interaction that becomes dominant when the temperature (and

thereby the mobility of the molecules) is reduced, and by an attractive electrostatic interaction between neighboring molecules that form an alternating pattern of antiparallel oriented vertical dipoles due to their ordered Sn-up/Sn-down pattern [11]. This second argument does not apply to the case of CuPc/Ag(111), since the molecules are planar, also after adsorption on the Ag surface. Therefore, the intermolecular attraction in the LT c-phase is reduced compared with the case of SnPc, which causes a reduced coverage range in which the c-phase is stable (up to 0.89 ML for CuPc compared to 0.94 ML for SnPc) and the molecular density is reduced by 10% (i.e. the SnPc c-phase is more densely packed than that of CuPc). The reduced attraction is also responsible for the fact that the c-phase is formed only at sufficiently high coverage. Upon cooling, when mobility is reduced, the molecules get trapped on their favorable adsorption sites (and also with a preferred in-plane orientation, as proven by the modulation of the outer ring in the LEED images). When the molecular density is high enough, this results in a densely packed ordered structure in which all molecules lie on one identical adsorption site and form the commensurate long-range ordered c-phase. When the density is lower, the molecules still adsorb on identical sites, but, due to the negligible intermolecular attractive forces, the molecules are located at randomly distributed adsorption sites on the surface, leading to a lack of long-range order.

At first sight, the SPA–LEED investigation of CuPc/Ag(111) yielded very similar results to the case of the previously investigated non-planar molecule SnPc [11]. The phase diagram looks very similar and the same effect of intermolecular repulsion at high coverages as well as the gas-like behavior in the low coverage regime were found. However, there are also major differences and new observations for the planar CuPc/Ag(111), which lead to an improved understanding of the adsorption behavior of the phthalocyanines in general.

First of all, the vertical dipole moment of the SnPc molecule can be ruled out as the driving force for the repulsive interaction, as discussed before. Even if the CuPc molecules are still slightly polarized (by the interaction with the surface), it is hardly conceivable that this small dipole moment causes the same effect on the structure formation as the much stronger moment of the non-planar SnPc molecules. This strongly supports the model of charge donation/backdonation that we suggested in our previous work [11].

Furthermore, we have pointed out that the vertical degree of freedom of the Sn atomic position, i.e. the tin-up and tin-down configuration, is the driving force for the formation of the commensurate low temperature phase of SnPc/Ag(111) with 2 molecules per unit cell on different adsorption sites. Such a structure cannot be observed in the case of the planar CuPc, which underlines the assumption that the tin-up and tin-down molecules interact differently with the substrate, leading to the occupation of inequivalent adsorption sites.

Thirdly, the fact that all ordered superstructures in the repulsive regime are of p.o.l. type strongly underlines the influence of the substrate on the repulsive effect. Molecules strictly glide along the [-110], [0-11] and [10-1] directions of the substrate when the coverage is changed. This allows us to conclude that the corrugation of the interface potential is relatively flat in these directions, implicating a low diffusion barrier.

Last but not least, the alignment of the molecular wings with the Ag(111) symmetry axes in the g-phases at LT is an interesting new aspect in the discussion of the adsorption geometry of the phthalocyanine molecules.

These results regarding the lateral structure of the overlayer—in particular, the molecule–molecule distance, which decreases with increasing coverage and hence reflects intermolecular repulsion—raises the question of correlations between lateral and vertical structure formation,

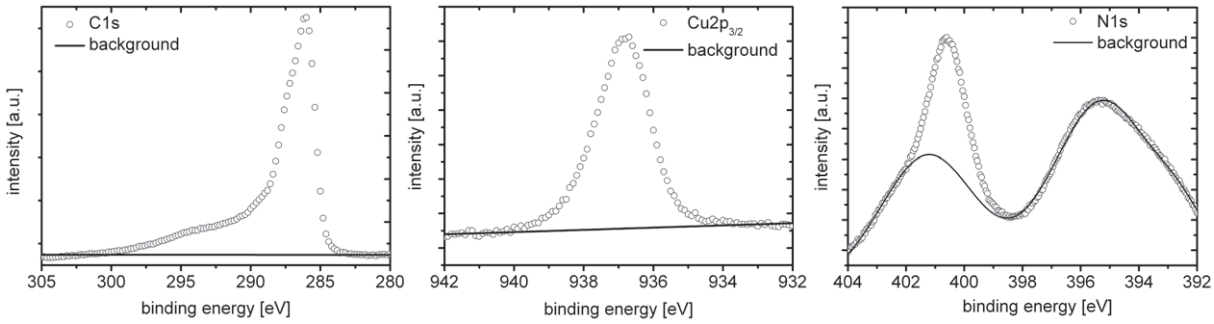


**Figure 7.** Exemplary photoelectron spectra and background subtraction of the C1s (left), $Cu2p_{3/2}$ (middle) and N1s (right) regions, recorded for the ML structure at 153 K.

the strength of the molecule–substrate bonding as well as the electronic structure. In order to investigate these aspects, we have performed NIXSW and UPS measurements.

## 4. Normal incidence x-ray standing wave (NIXSW) investigations

### *4.1. Data acquisition and raw data treatment*

XSW data sets of six different structures were recorded: (i) the ML structure at 300 K and (ii) at 153 K, (iii) a gaseous phase of 0.85 ML at 300 K, (iv) a structure with the same coverage at 139 K (commensurate phase), and (v) a gaseous phase with a lower coverage of 0.5 ML at 300 K and (vi) at 140 K (frozen gaseous phase). The films were prepared as described in section 2.1, their structure confirmed by LEED and the coverage determined using the normalized integral area of the C1s photoelectron signal, considering a linear background.

Beam damage in organic layers is a serious issue when performing XPS or XSW experiments. The main effect caused by the impact of photons or secondary electrons is a change to the chemical surrounding of individual species, e.g. by breaking of molecular bonds, which leads to defects or even a degradation of the entire organic film. This is most visible in changes in the XPS spectra like peak shifts, additional peaks or significant changes in intensities of individual peaks. In XSW, a degenerating film can also be identified by a reduction in the coherent fraction [6]. We checked for all these effects before taking the XSW data set and consequently avoided beam damage effectively by changing the irradiated spot on the sample after 20 min or less.

For the data set, only spots on the Ag(111) crystal with a very low mosaic spread were taken into account (reflectivity FWHM of 1.1 eV or smaller). This decreases the error of the reflectivity fit procedure and improves the quality of the data. Each reflectivity scan had 40 or 60 intervals and a width of 8 or 9 eV around the Bragg energy. At each point in the rocking curve, an XPS spectrum was recorded (C1s, $Cu2p_{3/2}$ or N1s, respectively), as well as the intensity of the incoming and Bragg reflected beam. For the C1s and $Cu2p_{3/2}$ spectra, it was sufficient to subtract a linear background (figure 7). However, in the N1s region, the background is dominated by Ag3d plasmons, which complicates the raw data treatment. Similar to our earlier work [12], we applied a background consisting of three Gaussians on a linear slope. The photoelectron yield $I(E)$ for each photon energy $E$ was then calculated by taking the integral peak intensity of the

**Table 2.** Summary of XSW results. The 'single' data refer to the average of the single measurement data points, and 'sum' stands for the analysis of summarized raw data. For details, see text.

| | | | C1s | | N1s | $Cu2p_{3/2}$ |
|---|---|---|---|---|---|---|
| Coverage (ML) | Temp. (K) | | Sum | Single | Single | Single |
| 0.50 | 300 | $P^H$ (Å) | 3.049(5) | 3.05(3) | 3.00(4) | 2.98(4) |
| | | $F^H$ | 0.631(13) | 0.62(8) | 0.65(8) | 0.95(8) |
| 0.85 | 300 | $P^H$ (Å) | 2.993(3) | 2.99(4) | 3.03(4) | 2.90(4) |
| | | $F^H$ | 0.627(2) | 0.63(4) | 0.69(8) | 0.70(8) |
| 1.00 | 300 | $P^H$ (Å) | 3.089(3) | 3.08(3) | 3.04(4) | 2.97(4) |
| | | $F^H$ | 0.475(5) | 0.48(6) | 0.57(8) | 0.53(8) |
| 0.50 | 153 | $P^H$ (Å) | 2.999(4) | 3.00(3) | 2.94(4) | 2.89(4) |
| | | $F^H$ | 0.754(13) | 0.75(6) | 0.94(8) | 0.91(8) |
| 0.85 | 140 | $P^H$ (Å) | 3.010(2) | 3.01(2) | 3.01(4) | 2.94(4) |
| | | $F^H$ | 0.647(5) | 0.63(7) | 0.85(8) | 0.81(8) |
| 1.00 | 140 | $P^H$ (Å) | 3.077(2) | 3.08(3) | 3.07(4) | 3.02(4) |
| | | $F^H$ | 0.545(5) | 0.54(5) | 0.64(8) | 0.58(8) |

corresponding background corrected XPS spectrum, normalized to the intensity of the incoming photon beam.

To fit the XSW profile $I(E)$, the reflectivity $R(E)$, the complex field amplitude $\sqrt{R(E)}$ and its phase $\nu(E)$ are needed. They were derived from fitting the corresponding rocking curve. To consider the intrinsic mosaicity of the crystal and the finite energy resolution of the beamline, a Gaussian energy broadening was further applied to the reflectivity fit procedure. This yielded the instrumental energetic spread, which was later also used in the XSW fitting routine of the photoelectron yield $I(E)$.

For a convenient illustration of the XSW results, we are going to use Argand diagrams in the following. Therein, the H-Fourier component of the spatial distributions of the individual adsorbate atomic species are shown as vectors in a polar diagram. The amplitude of the H-Fourier component (corresponding to the coherent fraction $F^H$) is displayed as the length of the vector with values between 0 and 1; its phase is plotted as a polar angle with values between 0 and $2\pi$ and it corresponds to the coherent position $P^H$.

### *4.2. Discussion of uncertainties*

The uncertainties and errors in an XSW experiment consist of statistical and systematic contributions and must be discussed in detail in order to make correct statements about the results. In order to evaluate the statistical uncertainty of the NIXSW measurement, we calculated the standard deviation of the fitting results of a series of single XSW scans. For the C1s yield of any of the different phases, this resulted in reliable values (see table 2), since this species shows the best signal-to-noise ratio (mainly for reasons of stoichiometry: C : N : Cu = 32 : 8 : 1). For coherent fractions and coherent positions, we found standard deviations between $\Delta F^H = 0.04$–$0.08$ and $\Delta P^H = 0.02$–$0.04$ Å, respectively, which is in good agreement with

uncertainties described in the literature (see, e.g., [14] or [12]). For the other species, we could not obtain reliable standard deviations from this statistical error treatment, since the single scans were too noisy. Therefore, we give the maximum numbers obtained for C1s as statistical uncertainties in this case ($\Delta F^{\mathrm{H}} = 0.08$, $\Delta P^{\mathrm{H}} = 0.04$ Å).

In order to justify this statistical treatment of uncertainties, we also evaluated the summarized signal of all individual scans. For this purpose, we sum all XPS spectra at each photon energy and evaluate the photoelectron yield of this 'sum measurement' (called 'sum' yield curves throughout the paper), together with the sum of the corresponding reflectivity curves. A least squares fit returns a 'sum' coherent position and coherent fraction, which shall lie well within the standard deviation of the average of the single measurements (see table 2). The rather small error of this 'sum' coherent position and coherent fraction represents the accuracy of the least square fit, but, as a realistic estimate of the uncertainty of the measurement, the standard deviation is the better value.

Finally, we would like to discuss the major systematic errors. The most prominent systematic error stems from an incorrect background subtraction in the XPS spectra. Since inelastically scattered bulk electrons dominate the background, this carries the XSW-signature of the substrate. A badly chosen background therefore causes a falsification of the measured signal by a bulk-like contribution. The resulting vector in the Argand diagram is then a sum of two vectors, the one representing the true signal from the species in question and the other stemming from the unwanted bulk-like contribution in the signal. The latter is a 'horizontal' vector (with polar angle zero) but with unknown length. The error occurs most strongly for the N1s spectra, since there the background is difficult to fit. In our case, since $P^{\mathrm{H}} \approx 0.25$ (i.e. the corresponding Argand vector is 'vertical' with a polar angle $\approx \pi/2$), a poor background subtraction would lead to an underestimation of the coherent position, since an added 'horizontal' vector would reduce the polar angle. For the Cu2p signal, the major systematic error is the unknown non-dipolar parameter $\Delta$, which in this paper was set to a value similar to those for the other species ($\Delta = -0.21$). This parameter influences the phase shift in the cosine term of the XSW formula and hence—if it is incorrect—leads to a small over- or underestimation of the coherent position. For the Cu2p signal from the 1 ML structure at 300 K, the change of $\Delta$ from $-0.21$ to 0 leads to a rise in $P^{\mathrm{H}}$ of 0.013 Å, so the error is relatively small.

### *4.3. Results of the XSW investigations*

The results of the XSW investigations are shown in figures 8–10. In the upper half of each figure, the sum yield curves are shown with their corresponding fit results. In the lower half, the Argand diagram is shown, containing the fit results of the single-scan curves (open symbols) and their statistical average (filled symbols). Numerical values are shown in table 2. Note that the results of the sum curves lie well inside the uncertainties obtained from the single data evaluation.

Three major conclusions can be drawn from analyzing these data. The most important is a general trend to smaller adsorption heights and higher coherent fractions when the coverage is reduced. At low temperature, this effect is more pronounced than at room temperature (figures 11 and 12). Obviously, this effect is correlated with the change in intermolecular (lateral) distance, which was found in SPA–LEED (see above). We will discuss this point in detail in section 6. Furthermore, all bonding distances are smaller than the sum of the van der Waals radii of the involved elements (values from [32]: Ag: $r_{\mathrm{W}} = 1.72$ Å, C: $r_{\mathrm{W}} = 1.77$ Å, N: $r_{\mathrm{W}} = 1.55$ Å, Cu: $r_{\mathrm{W}} = 1.4$ Å). This implicates an overlap of occupied molecular states with

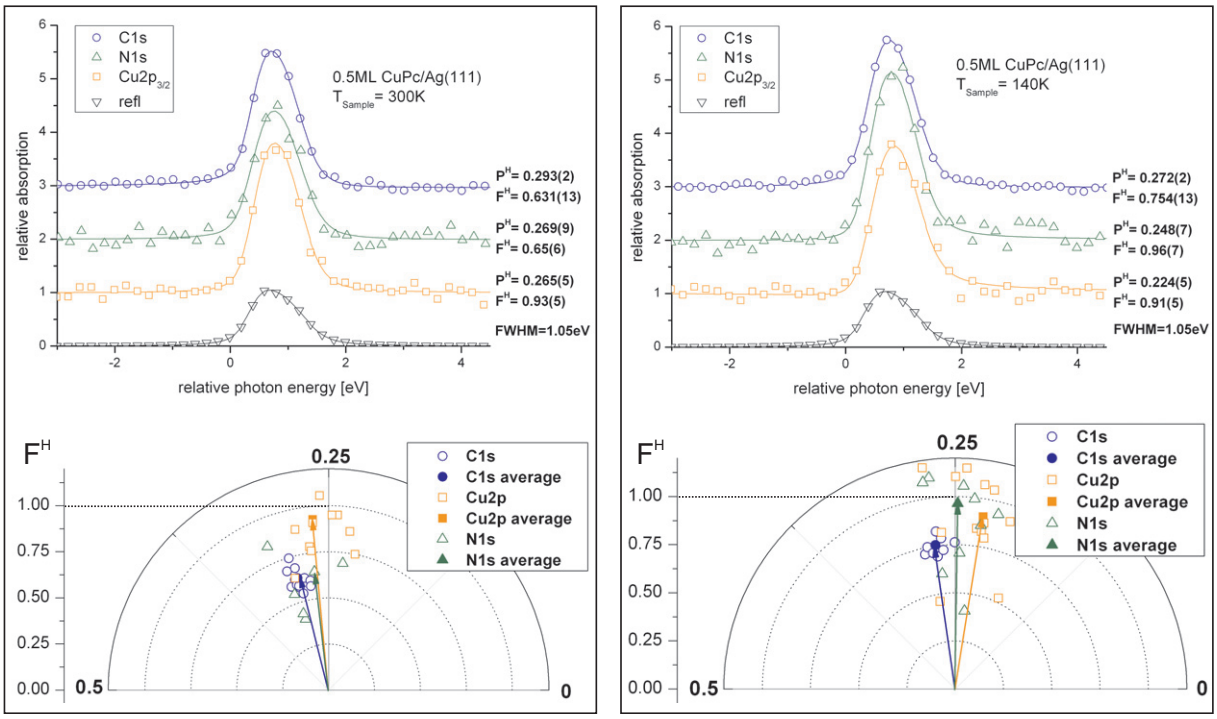


**Figure 8.** Photoelectron sum yield curves and Argand representation of the results obtained from the 0.5 ML phase of CuPc/Ag(111) at 300 K (left) and 140 K (right).

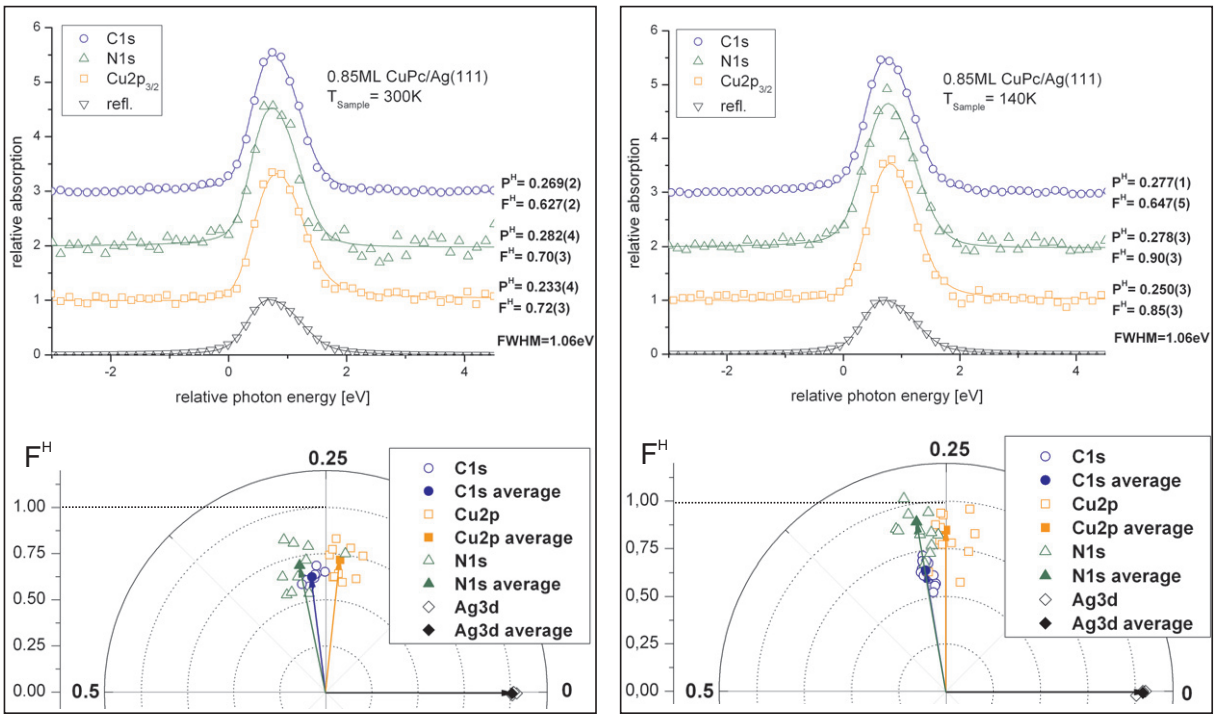


**Figure 9.** Photoelectron sum yield curves and Argand representation of the results obtained from the 0.85 ML phase of CuPc/Ag(111) at 300 K (left) and 140 K (right).

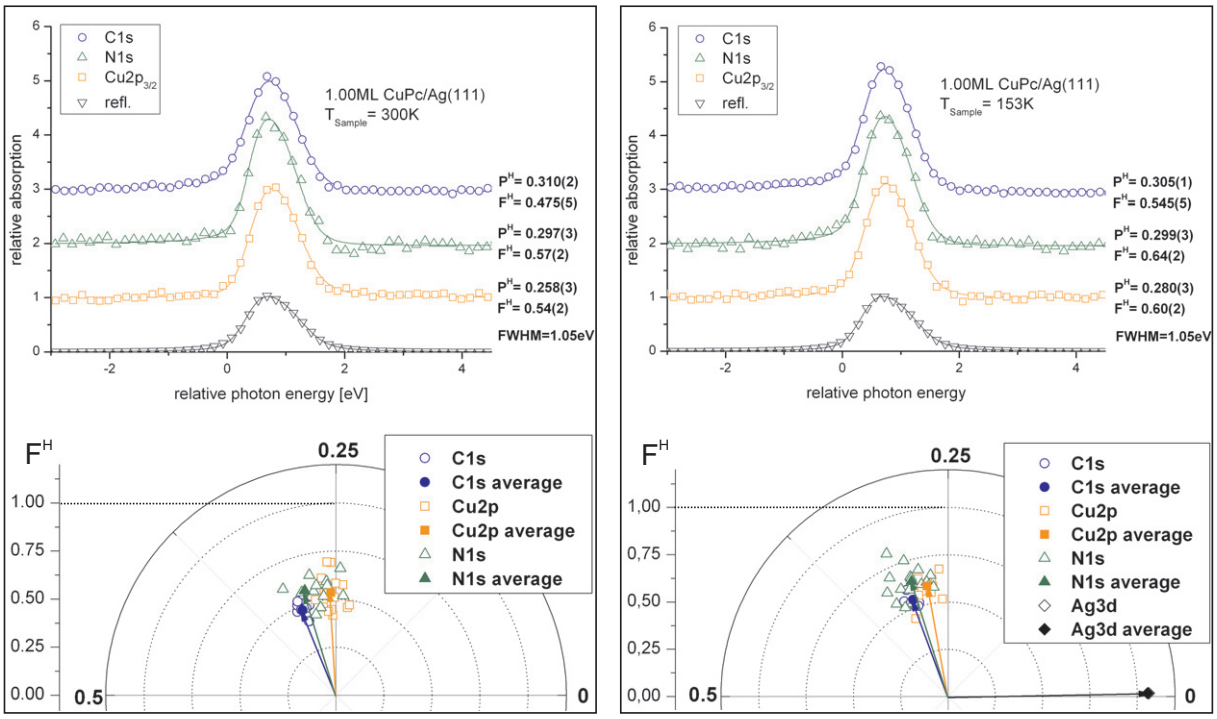


**Figure 10.** Photoelectron sum yield curves and Argand representation of the results obtained from the 1.0 ML phase of CuPc/Ag(111) at 300 K (left) and 153 K (right).

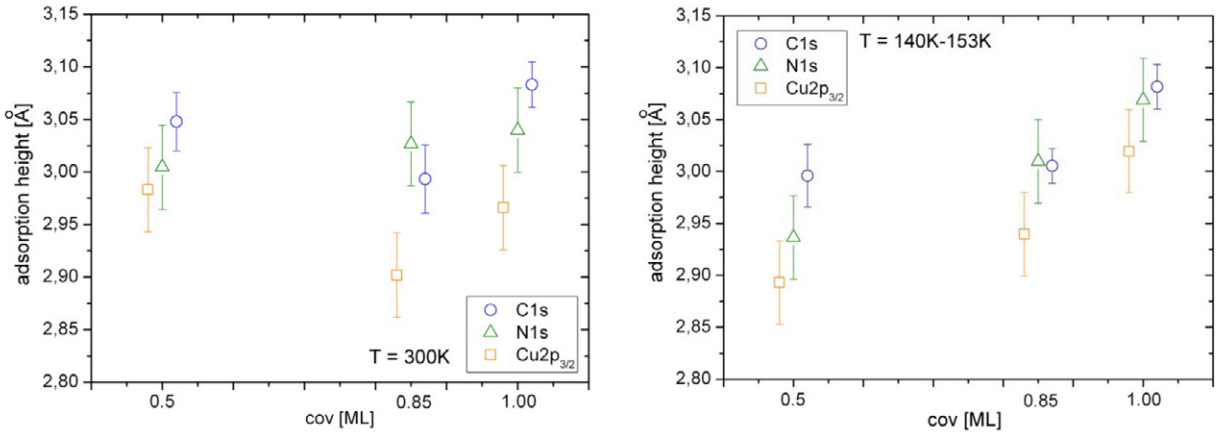


**Figure 11.** Comparison of adsorption heights for different coverages. A trend towards larger adsorption heights with increasing coverage can be seen, in particular at LT.

the electron density of the substrate, and consequently an exchange of electronic charge, i.e. chemisorption.

The second conclusion drawn from the XSW results is that the molecule is slightly distorted. The copper atom is in all cases located below the nitrogen atoms, which—for their part—in many cases lie below the molecular plane of carbon atoms. Even though the distortion

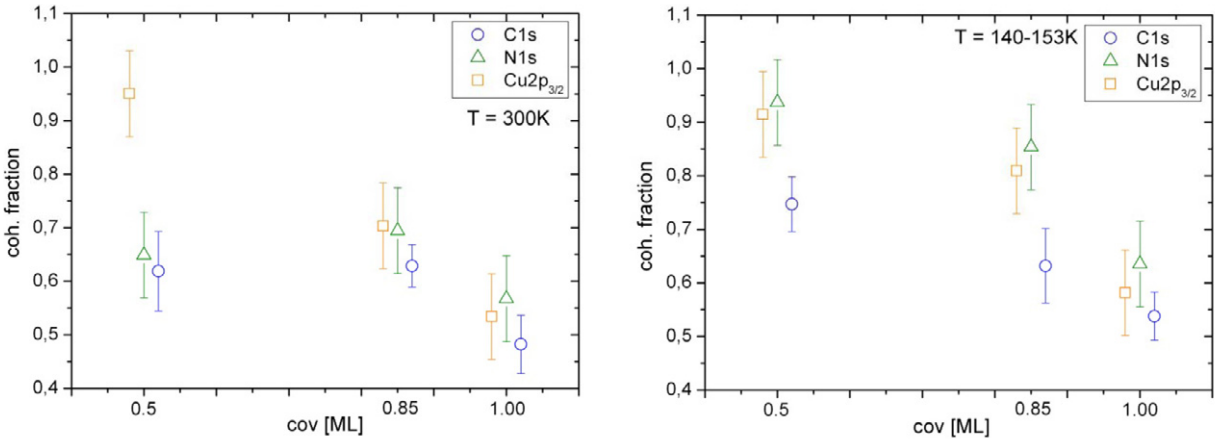


**Figure 12.** Comparison of coherent fractions for different coverages. A trend towards smaller coherent fractions with increasing coverage can be seen, in particular at LT.

is just within the error bars of the measurement, it is a very noticeable systematic trend in all independently investigated phases. We believe that this trend holds even in light of the discussion of possible systematic errors for the N1s and $Cu2p_{3/2}$ species. The deviation from the planar geometry points towards an interaction of the nitrogen and metal atoms with the substrate, which was—in a much stronger manner—also observed for the non-planar SnPc molecule [11] and related metal-porphyrine molecules on Ag(111) [33, 34].

The third aspect that can be found in the XSW data is a lower coherent fraction measured at room temperature compared to low temperature for phases having the same coverage. For the ML structure, this effect is small (within the error bars: $\Delta F^{H} \leqslant 0.1$), but at 0.5 ML it becomes significant, especially for nitrogen ($\Delta F^{H} \leqslant 0.3$). We attribute this observation (at least partly) to the excitation of out-of-plane vibration modes at elevated temperatures. Since this effect should be similar at all coverages, it probably causes a difference of approximately $\Delta F^{H} \leqslant 0.1$, which is observed for all coverages. The additional effect in the lower sub-ML regime is probably caused by an additional vertical ordering mechanism (such as a stronger interaction with the surface), which occurs at lower temperatures and goes along with commensurism (at medium coverages) and an azimuthal alignment of the molecules with the substrate (at low coverages), as was observed by SPA–LEED. Other effects and artifacts, such as a falsified N1s signal due to bad background subtraction or second-layer molecules at high coverages, can widely be excluded (the first due to the actual coherent position of all species—about 0.25—at which a bad background subtraction has minimal effect on the coherent fraction, the latter since second-layer molecules were effectively avoided by annealing the sample for 20 min at the multilayer desorption temperature of 533 K).

## 5. UPS investigations

The left part of figure 13 shows the valence structure of 0.9 ML CuPc on Ag(111) at 80 K measured at an emission angle of 50°. The highest occupied molecular orbital (HOMO) state lies 1.25 eV below the Fermi edge and shows an asymmetric peak shape caused by a vibronic progression that was already observed for CuPc on HOPG [35]–[37] and in the

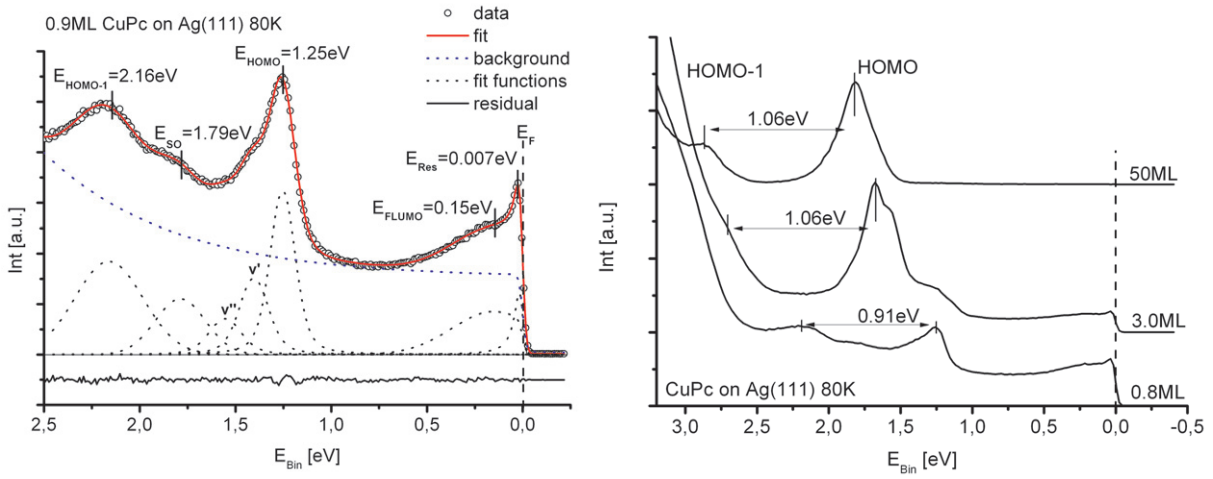


**Figure 13.** Left: valence structure of 0.9 ML CuPc/Ag(111) at 80 K. Background and fit functions are shown as dashed lines. Right: evolution of the energetic difference between HOMO and HOMO-1 at higher coverage. For details, see text.

CuPc gas phase [38]. From our data, we obtained a separation energy of these progression peaks of 150 meV similar to the CuPc gas phase measurements. However, the intensity ratio of the progressions relative to the HOMO peak is, for similar emission angles, higher for CuPc on Ag(111) compared with CuPc/HOPG [36] or with the gas phase, which indicates a stronger coupling of the HOMO band with vibrational excitations in the photoionization process.

The HOMO-1 level is located at a binding energy of 2.16 eV and shows an additional feature at 1.79 eV, which we identify as a HOMO-1 split off (SO) band. The SO state occurs only in the sub-ML regime but not for higher coverages (see right part of figure 13), and hence originates from the molecule–substrate interaction. The intensity ratio of HOMO-1 and SO peaks changes when the coverage is varied in the sub-ML regime. However, the sum of both peaks reflects the nominal coverage. This underlines the common origin of these two peaks. When the coverage is increased towards the multilayers, the distance between HOMO and HOMO-1 increases from 0.91 to 1.09 eV. This further indicates that these states participate in the chemisorptive bonding.

Another striking feature in the UPS data is located at a binding energy of 0.15 eV close to the Fermi edge and is identified as a partially filled 'former' lowest unoccupied molecular orbital (F-LUMO). This originates from a charge transfer from substrate to molecule and was earlier observed for e.g. PTCDA/Ag(111) [5], NTCDA/Ag(111) [39] and SnPc/Ag(111) [40]. An additional sharp spectral feature can be observed close to the Fermi level. Whereas usually the molecular states appear in the PE spectra as peaks with line widths clearly above 100 meV, this feature has an FWHM of less than 30 meV at low temperatures. However, a detailed analysis [41] shows that this peak is clearly derived from the F-LUMO and, furthermore, bears some indications of the importance of many-body effects in this hybrid system. In particular, it should be noted that this peak is not caused by the Shockley-type surface state of the Ag(111) substrate [42], which is shifted far above the Fermi level due to the interaction with the molecular adsorbate [43, 44].

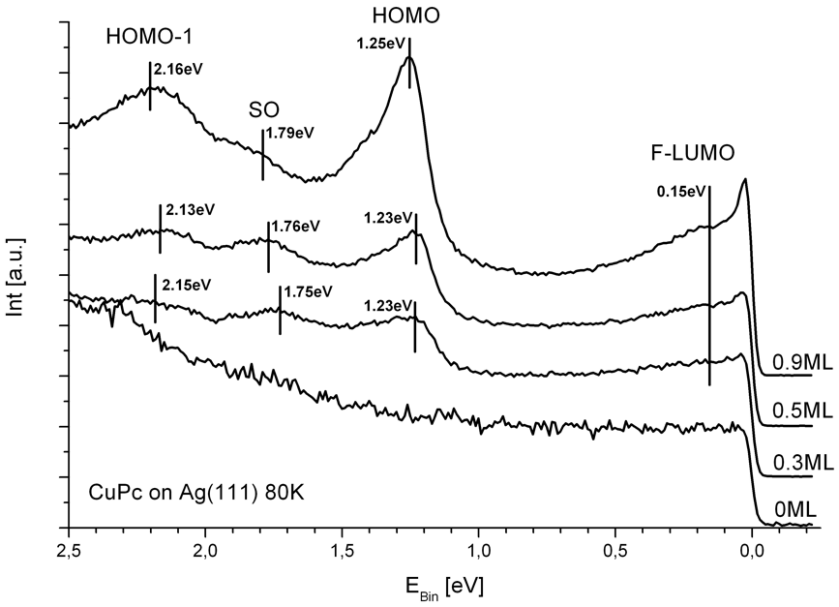


**Figure 14.** UPS spectra at different coverages, indicating the shifts of HOMO-1, HOMO and F-LUMO peaks with increasing coverage.

In the UPS data recorded for a *multilayer* film with a nominal thickness of 3 ML (figure 13, right), three components can be seen in the HOMO peak. These correspond to the HOMO peak positions for an ML structure (1.25 eV), the second layer (1.56 eV) and the third layer (1.71 eV). The shift in binding energies in the *multilayer* results from the weakening of the coupling of photoelectron holes with the electronic system of the substrate. For films thicker than three layers, no further shift can be detected, i.e. the molecules are then effectively decoupled from the metallic substrate.

Figure 14 shows UPS spectra at different coverages, which illustrate the changes of the valence structure in the sub-ML regime. The HOMO and SO levels show with increasing coverage a small shift of 20 and 40 meV towards higher binding energies, respectively. If a similar effect was present in the F-LUMO, it could not be detected due to its very broad peak structure. Correlating this observation with the XSW and SPA–LEED results shows that the shift of the molecular orbitals of CuPc/Ag(111) to higher binding energies corresponds to a weaker bonding to the substrate combined with a higher molecular density. This is in strong contrast with the observation of PTCDA/Ag(111) [1, 4], where the phase transition from the stronger bonded LT phase with lower density to the weaker bonded RT phase with higher density leads to a valence level shift to lower binding energies.

## 6. Conclusions

The adsorption of CuPc molecules and the formation of a variety of lateral structures can be understood as the result of a minimization of the interface potential energy, under some specific boundary conditions. An important aspect that enables this interesting adsorption behavior is the D4h (respectively, $\frac{4}{m}mm$) symmetry of the molecule, which is responsible for a vanishing intrinsic electrostatic moment. Hence, there is no strong intermolecular attractive force that

usually leads to the formation of islands in the sub-ML coverage regime. At low coverages, this also allows the molecules to move (and rotate) freely on the surface (like in a 2D gas) and, when the temperature is reduced, to find their energetically most favorable adsorption positions individually, without being trapped by the interaction with other molecules. At 153 K, movements and rotations are inhibited. SPA–LEED and NIXSW measurements provided experimental evidence that the energetic minimum corresponds to a specific adsorption site, a maximized nearest-neighbor distance and a minimized adsorption height above the surface. This leads to the smallest binding energies we found in UPS for the HOMO and SO states. Intramolecular scattering indicates an alignment of the molecular axis along the high-symmetry directions of the substrate, since this apparently leads to an optimized overlap of molecular orbitals with the electronic states of the surface. This better overlap of wavefunctions is also indicated by higher coherent fractions of nitrogen and carbon atoms and, in particular, by shorter bonding distances to the substrate compared to RT. When comparing with geometries obtained theoretically, one has to consider these experimental data (not the ML data), since these are measured for a rather diluted phase and hence reflect the interaction of 'isolated' molecules with the surface.

At increasing coverage (up to ≈0.85 ML) and at low temperature, the CuPc molecules remain in their favorable adsorption sites and fill up the surface homogeneously. Even before the surface is completely covered, they arrange themselves in close-packed islands with the nearest-neighbor distance below 16 Å and form a long-range ordered commensurate superstructure. Compared to the 0.5 ML case, the bonding to the substrate is weaker, leading to an elongated vertical distance. This goes along with a reduced electronic overlap due to a sterically induced azimuthal misalignment of the molecules in the densely packed structure. The competing effect between nearest neighbors for the charge transfer with the substrate possibly also plays a role, as discussed earlier [11].

The commensurate phase represents the low-coverage limit of a series of p.o.l. phases that occur between 0.89 and 1.0 ML. The structural changes in this region run continuously up to their upper limit, the ML structure. For the latter, the weakest bonding, the lowest coherent fraction and the highest binding energies for SO and HOMO states were found at both low temperature and room temperature. The interface potential energy model by Mannsfeld *et al* [28, 30] can nicely explain the p.o.l. character of these phases by the overlap of the molecular wavefunctions with substrate states and neighboring molecules. Adding further molecules to the surface increases the total binding energy to the cost of the binding energy of individual molecules (since they are forced away from their energetically favorable adsorption sites) and to the cost of an increasing Pauli repulsion between neighboring molecules, since their electronic states start overlapping. As long as the energy balance is a total gain, further molecules adsorb in the first layer and cause a more compressed structure. As soon as the balance turns negative, the growth of the second layer starts. It is remarkable that the self-organization in the molecular film necessitates a reorganization of the entire film, with the superlattice always pointing to substrate lattice lines along the [-110], [-101] or [0-11] directions. Regarding the discussion above, it can be assumed that the molecular axis also tends to be aligned along these directions, apart from a slight misalignment due to sterical reasons in the close-packed structure. Finally, we can conclude that the global binding energy of the adsorbate layer, which drives the structure formation in this case, turns out to be responsible for an intermolecular *repulsion*, because neighboring molecules compete for better adsorption sites and larger molecular binding energy. We hope that our comprehensive experimental data

contribute to a fundamental understanding of this interesting system, also on a more quantitative level that can be reached using quantum chemical calculations.

## 7. Summary

We have presented a complete structural study of the adsorption of CuPc on Ag(111) in the sub-ML range. The lateral and vertical structures were investigated by SPA–LEED and NIXSW, respectively, and complemented by UPS measurements of the electronic valence structure. Similar to the case of SnPc/Ag(111), three major regions were found: a series of long-range ordered molecular superstructures with p.o.l. coincidence at high coverages; a disordered phase below 0.89 ML; and a commensurate superstructure that occurs at low temperatures between 0.75 and 0.89 ML and represents the condensed disordered phase. The NIXSW analysis showed a general trend of larger adsorption heights with increasing coverage, indicating a weakening of the bonding to the substrate caused by more dense packing on the surface. This is in agreement with UPS measurements that showed adsorbate-induced features (a partly filled former LUMO and a HOMO-1 SO band). Global energy optimization is responsible for this behavior and, in contrast to commonly known organic adsorbate systems, causes intermolecular repulsion in this case.

## Acknowledgments

We acknowledge financial support from the Deutsche Forschungsgemeinschaft (KU 1531/2-1, GK 1221 and FOR 1162) and from the ESRF, Grenoble, France.

## References

[1] Kilian L *et al* 2008 Role of intermolecular interactions on the electronic and geometric structure of a large pi-conjugated molecule adsorbed on a metal surface *Phys. Rev. Lett.* **100** 136103

[2] Kilian L, Stahl U, Kossev I, Sokolowski M, Fink R and Umbach E 2008 The commensurate-to-incommensurate phase transition of an organic monolayer: a high resolution LEED analysis of the superstructures of NTCDA on Ag(111) *Surf. Sci.* **602** 2427–34

[3] Hauschild A, Karki K, Cowie B C C, Rohlfing M, Tautz F S and Sokolowski M 2005 Molecular distortions and chemical bonding of a large pi-conjugated molecule on a metal surface *Phys. Rev. Lett.* **94** 036106

[4] Hauschild A, Temirov R, Soubatch S, Bauer O, Schöll A, Cowie B C C, Lee T-L, Tautz F S and Sokolowski M 2010 Normal-incidence x-ray standing-wave determination of the adsorption geometry of PTCDA on Ag(111): comparison of the ordered room-temperature and disordered low-temperature phases *Phys. Rev.* B **81** 125432

[5] Zou Y, Kilian L, Schöll A, Schmidt T, Fink R and Umbach E 2006 Chemical bonding of PTCDA on Ag surfaces and the formation of interface states *Surf. Sci.* **600** 1240–51

[6] Henze S K M, Bauer O, Lee T L, Sokolowski M and Tautz F S 2007 Vertical bonding distances of PTCDA on Au(111) and Ag(111): relation to the bonding type *Surf. Sci.* **601** 1566–73

[7] Tautz F S 2007 Structure and bonding of large aromatic molecules on noble metal surfaces: the example of PTCDA *Progr. Surf. Sci.* **82** 479–520

[8] Duhm S, Gerlach A, Salzmann I, Broeker B, Johnson R L, Schreiber F and Koch N 2008 PTCDA on Au(111), Ag(111) and Cu(111): correlation of interface charge transfer to bonding distance *Org. Electron.* **9** 111–8

[9] Romaner L, Nabok D, Puschnig P, Zojer E and Ambrosch-Draxl C 2009 Theoretical study of PTCDA adsorbed on the coinage metal surfaces, Ag(111), Au(111) and Cu(111) *New J. Phys.* **11** 053010

[10] McKeown N B 1998 *Phthalocyanine Materials* (Cambridge: Cambridge University Press)
[11] Stadler C, Hansen S, Kröger I, Kumpf C and Umbach E 2009 Tuning intermolecular interaction in long-range-ordered submonolayer organic films *Nature Phys.* **5** 153–8
[12] Stadler C, Hansen S, Pollinger F, Kumpf C, Umbach E, Lee T L and Zegenhagen J 2006 Structural investigation of the adsorption of SnPc on Ag(111) using normal-incidence x-ray standing waves *Phys. Rev.* B **74** 035404
[13] Horn von Hoegen M 1999 Growth of semiconductor layers studied by spot profle analysing low energy electron diffraction, part I *Z. Kristallogr.* **214** 591–629, part II *ibid*. 684–721
[14] Gerlach A, Sellner S, Schreiber F, Koch N and Zegenhagen J 2007 Substrate-dependent bonding distances of PTCDA: a comparative x-ray standing-wave study on Cu(111) and Ag(111) *Phys. Rev.* B **75** 045401
[15] Stanzel J, Weigand W, Kilian L, Meyerheim H L, Kumpf C and Umbach E 2004 Chemisorption of NTCDA on Ag(111): a NIXSW study including non-dipolar and electron-stimulated effects *Surf. Sci.* **571** L311–8
[16] Stadler C, Hansen S, Schöell A, Lee T-L, Zegenhagen J, Kumpf C and Umbach E 2007 Molecular distortion of NTCDA upon adsorption on Ag(111): a normal incidence x-ray standing wave study *New J. Phys.* **9** 50
[17] Gerlach A, Schreiber F, Sellner S, Dosch H, Vartanyants I A, Cowie B C C, Lee T L and Zegenhagen J 2005 Adsorption-induced distortion of F16CuPc on Cu(111) and Ag(111): an x-ray standing wave study *Phys. Rev.* B **71** 205425
[18] Koch N *et al* 2008 Adsorption-induced intramolecular dipole: correlating molecular conformation and interface electronic structure *J. Am. Chem. Soc.* **130** 7300–4
[19] Mercurio G *et al* 2010 Structure and energetics of azobenzene on Ag(111): benchmarking semiempirical dispersion correction approaches *Phys. Rev. Lett.* **104** 036102
[20] Batterman B W and Cole H 1964 Dynamical diffraction of x-rays by perfect crystals *Rev. Mod. Phys.* **3** 681–717
[21] Zegenhagen J 1993 Surface-structure determination with X-ray standing waves *Surf. Sci. Rep.* **18** 199–271
[22] Woodruff D P 1998 Normal incidence X-ray standing wave determination of adsorbate structures *Prog. Surf. Sci.* **57** 1–60
[23] Vartanyants I A and Zegenhagen J 1999 Photoelectric scattering from an X-ray interference field *Solid State Commun.* **113** 299–320
[24] Lee J J, Fisher C J, Woodruff D P, Roper M G, Jones R G and Cowie B C C 2001 Non-dipole effects in photoelectron-monitored X-ray standing wave experiments: characterisation and calibration *Surf. Sci.* **494** 166–82
[25] Hoshino A, Isoda S, Kurata H and Kobayashi T 1994 Scanning tunneling microscope contrast of Perilene-3,4,9,10-tetracarboxylic-dianhydride on graphite and its application to the study of epitaxy *J. Appl. Phys.* **76** 4113–20
[26] Hooks D E, Fritz T and Ward M D 2001 Epitaxy and molecular organization on solid substrates *Adv. Mater.* **13** 227
[27] Mannsfeld S, Törker M, Schmitz-Hübsch T, Sellam F, Fritz T and Leo K 2001 Combined LEED and STM study of PTCDA growth on reconstructed Au(1 1 1) and Au(1 0 0) single crystals *Org. Electron.* **2** 121–34
[28] Mannsfeld S C B and Fritz T 2005 Understanding organic–inorganic heteroepitaxial growth of molecules on crystalline substrates: experiment and theory *Phys. Rev.* B **71** 235405
[29] Strohmaier R, Ludwig C, Petersen J, Gompf B and Eisenmenger W 1996 STM investigations of NTCDA on weakly interacting substrates *Surf. Sci.* **351** 292–302
[30] Mannsfeld S C B and Fritz T 2004 Analysis of the substrate influence on the ordering of epitaxial molecular layers: the special case of point-on-line coincidence *Phys. Rev.* B **69** 075416
[31] Frisch M J *et al* 2004 *Gaussian 03,* revision C.02 (Wallingford, CT: Gaussian)
[32] Bondi A 1964 Van der Waals volumes + radii *J. Phys. Chem.* **68** 441

[33] Lukasczyk T, Flechtner K, Merte L R, Jux N, Maier F, Gottfried J M and Steinrück H P 2007 Interaction of cobalt(II) tetraarylporphyrins with a Ag(111) surface studied with photoelectron spectroscopy *J. Phys. Chem.* C **111** 3090–8

[34] Flechtner K, Kretschmann A, Steinrück H P and Gottfried J M 2007 NO-induced reversible switching of the electronic interaction between a porphyrin-coordinated cobalt ion and a silver surface *J. Am. Chem. Soc.* **129** 12110

[35] Kera S, Yamane H, Sakuragi I, Okudaira K K and Ueno N 2002 Very narrow photoemission bandwidth of the highest occupied state in a copper-phthalocyanine monolayer *Chem. Phys. Lett.* **364** 93–8

[36] Kera S, Yamane H and Ueno N 2009 First-principles measurements of charge mobility in organic semiconductors: valence holevibration coupling in organic ultrathin films *Prog. Surf. Sci.* **84** 135–54

[37] Ueno N, Kera S, Sakamoto K and Okudaira K K 2008 Energy band and electron-vibration coupling in organic thin films: photoelectron spectroscopy as a powerful tool for studying the charge transport *Appl. Phys.* A **92** 495–504

Ueno N, Kera S, Sakamoto K and Okudaira K K 2007 *15th Int. Conf. on Vacuum Ultraviolet Radiation Physics* (*Berlin, Germany, 29 July–3 August 2007*)

[38] Evangelista F, Carravetta V, Stefani G, Jansik B, Alagia M, Stranges S and Ruocco A 2007 Electronic structure of copper phthalocyanine: an experimental and theoretical study of occupied and unoccupied levels *J. Chem. Phys.* **126** 124709

[39] Bendounan A, Forster F, Schöll A, Batchelor D, Ziroff J, Umbach E and Reinert F 2007 Electronic structure of 1 ML NTCDA/Ag(111) studied by photoemission spectroscopy *Surf. Sci.* **601** 4013–7

Bendounan A, Forster F, Schöll A, Batchelor D, Ziroff J, Umbach E and Reinert F 2006 *24th European Conf. on Surface Science* (*ECOSS-24*) (*Paris, France, 4–8 September 2006*)

[40] Häming M, Scheuermann C, Schöll A, Reinert F and Umbach E 2009 Coverage dependent organic–metal interaction studied by high-resolution core level spectroscopy: SnPc (sub)monolayers on Ag(111) *J. Electron Spectrosc. Relat. Phenom.* **174** 59–64

[41] Ziroff J, Hame S, Kochler M, Bendounan F, Forster A and Reinert F 2010 submitted

[42] Reinert F, Nicolay G, Schmidt S, Ehm D and Hüfner S 2001 Direct measurements of the L-gap surface states on the (111) face of noble metals by photoelectron spectroscopy *Phys. Rev.* B **63** 115415

[43] Forster F, Bendounan A, Ziroff J and Reinert F 2006 Systematic studies on surface modifications by ARUPS on Shockley-type surface states *Surf. Sci.* **600** 3870

[44] Schwalb C H, Sachs S, Marks M, Schöll A, Reinert F, Umbach E and Höfer U 2008 Electron lifetime in a Shockley-type metal–organic interface state *Phys. Rev. Lett.* **101** 146801